Supplementary Material

1 ADDITIONAL CVD SYNTHESIS DETAILS

The crucial physical parameters that control CVD diamond synthesis include the density of surface radical sites, the rate of CH_x addition relative to etching by H atoms, and the near-surface NH_x (or CN)/CH_x ratio (Edmonds et al., 2021). The mapping of CVD process conditions (such as power, gas flows, and surface temperature) to these parameters is dependent on the specific CVD reactor design (Edmonds et al., 2021; Gracio et al., 2010; Cuenca et al., 2022). For the diamonds studied here, Element Six's proprietary and non-disclosed reactor design is used; and therefore it is not possible to generalize for users of other reactor platforms.

2 STRAIN AND STRESS MAPS

The NV electronic spin Hamiltonian contains spin-strain coupling terms, including longitudinal (M_z) and transverse (M_x, M_y) components (Barfuss et al., 2019). Under a strong bias magnetic field ($B\uparrow \gtrsim 10\ G$), the longitudinal component M_z dominates NV spin resonance frequency shifts, and transverse contributions can be neglected (Kehayias et al., 2019). By resolving NV spin transitions corresponding to the four NV orientations in the diamond lattice, the spin stress terms $M_{z,i}$ for each orientation i are experimentally determined using continuous-wave optically detected magnetic resonance (CW-ODMR) measurements, as described in Kehayias et al. (2019). Representative spatial maps of these terms across diamond sample 10 are shown in Fig. S1.

Additionally, from these strain measurements, the stress tensor components of the diamond – comprising diagonal terms ($\sigma_{diag} = \sigma_{xx} + \sigma_{yy} + \sigma_{zz}$) and off-diagonal shear terms (σ_{xy}, σ_{yz}, σ_{xz}) – can be uniquely determined. The calculation method is detailed in Ref. Kehayias et al. (2019) and the results are also shown in Fig. S1.

3 RAMSEY MEASUREMENT AT HIGH-BIREFRINGENCE LOCATION

As shown in the main text (Fig. 2), sample 10 contains two regions with elevated birefringence, indicating higher strain variation. To illustrate the effect of such inhomogeneity on NV ensemble properties, we perform a single-quantum ( ) Ramsey measurement at a spot within area B. The extracted dephasing time is $T^*_{2,\mathrm{SQ}} = 5.1(6)\ \mu$s, significantly shorter than the spin-bath-limited value. In contrast, a double-quantum (DQ) Ramsey measurement at this same spot, which is insensitive to longitudinal strain and temperature variations (Hart et al., 2021), yields $T^*_{2,\mathrm{DQ}} = 8.6(5)\ \mu$s. This value is approximately half of the SQ dephasing time observed in low-birefringence regions (main text, Fig. 3), consistent with the doubled gyromagnetic ratio and increased sensitivity to spin-bath noise of DQ measurements.

4 SPIN-BATH-LIMITED NV SPIN DEPHASING TIME

The spin-bath-limited NV spin dephasing time ($T^*_{2,\mathrm{bath}}$) can be estimated using the following relation (Barry et al., 2020):

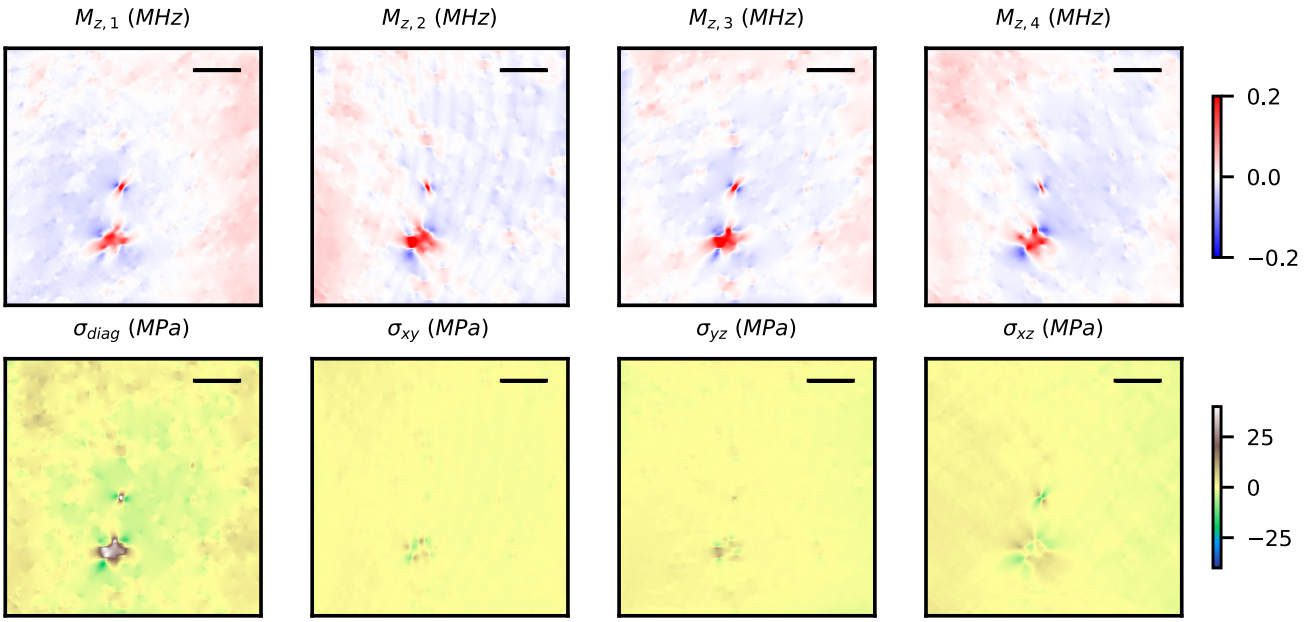


Figure S1. Spatial maps of experimentally determined NV spin-strain coupling terms (M_z) for each of four NV orientations and derived diamond stress tensors components σ across the entire diamond sample 10. Scale bars: $500\,\mu$m

$$\begin{aligned}\frac{1}{T^*_{2,\text{bath}}} &= \frac{1}{T^*_{2,[\text{N}_\text{s}^0]}} + \frac{1}{T^*_{2,[^{13}\text{C}]}} + \frac{1}{T^*_{2,\text{NV-NV}}} \\ &\approx A_{\text{N}_\text{s}^0}[\text{N}_\text{s}^0] + A_{^{13}\text{C}}[^{13}\text{C}] + \zeta_{\parallel} A_{\text{NV}^-_{\parallel}}[\text{NV}^-_{\parallel}] + \zeta_{\nparallel} A_{\text{NV}^-_{\nparallel}}[\text{NV}^-_{\nparallel}],\end{aligned} \tag{S1}$$

where the scaling constants are $A_{\text{N}_\text{s}^0} = 0.101\,\mu\text{s}^{-1}\text{ppm}^{-1}$, $A_{^{13}\text{C}} = 0.1\,\text{ms}^{-1}\text{ppm}^{-1}$, $A_{\text{NV}^-_{\parallel}} = 0.247\,\mu\text{s}^{-1}\text{ppm}^{-1}$ and $A_{\text{NV}^-_{\nparallel}} = 0.165\,\mu\text{s}^{-1}\text{ppm}^{-1}$. Here, $[\text{NV}^-_{\parallel}]$ represents the concentration of negatively-charged NV centers (NV^-) aligned along the sensing axis, while $[\text{NV}^-_{\nparallel}]$ corresponds to the concentration of NV centers oriented along other crystal axes. For our experimental study, the bias magnetic field aligns with a single NV crystal axis, resulting in $[\text{NV}^-_{\parallel}] \approx \frac{1}{3}[\text{NV}^-_{\nparallel}]$. For the sensing axis and other axes, the dimensionless correction factor ζ accounts for the incomplete polarization of NV^- spins into the $m_s = 0$ state. We optimize laser polarization such that NV centers aligned along two axes are predominantly excited, with one orientation used for sensing. Thus, we approximate $\zeta_{[\text{NV}^-_{\parallel}]} \approx 0$. Determining $\zeta_{[\text{NV}^-_{\nparallel}]}$ is complicated due to unequal laser excitation intensities and polarizations along the three non-sensing NV orientations under epi-illumination conditions; as a conservative estimate for the NV-NV interaction-limited $T^*_{2,\text{NV-NV}}$, we assume partial non-sensing NV spin polarization with $\zeta_{\nparallel} = 0.5$.

Before electron irradiation and annealing of the ten low-$[\text{N}_\text{s}^0]$ diamond samples, the substitutional nitrogen concentration is measured to be $[\text{N}_\text{s}^{0,\text{as-grown}}] \approx 0.8\,\text{ppm}$ via UV-Vis absorption (Edmonds et al., 2021). After processing, the total NV concentration is 0.39(2) ppm determined by UV-Vis absorption (Edmonds et al., 2021), with approximately 20% of NVs in the negatively charged (NV^-) state (as determined from the PL emission spectrum decomposition technique, see main text). Formation of NV centers consumes

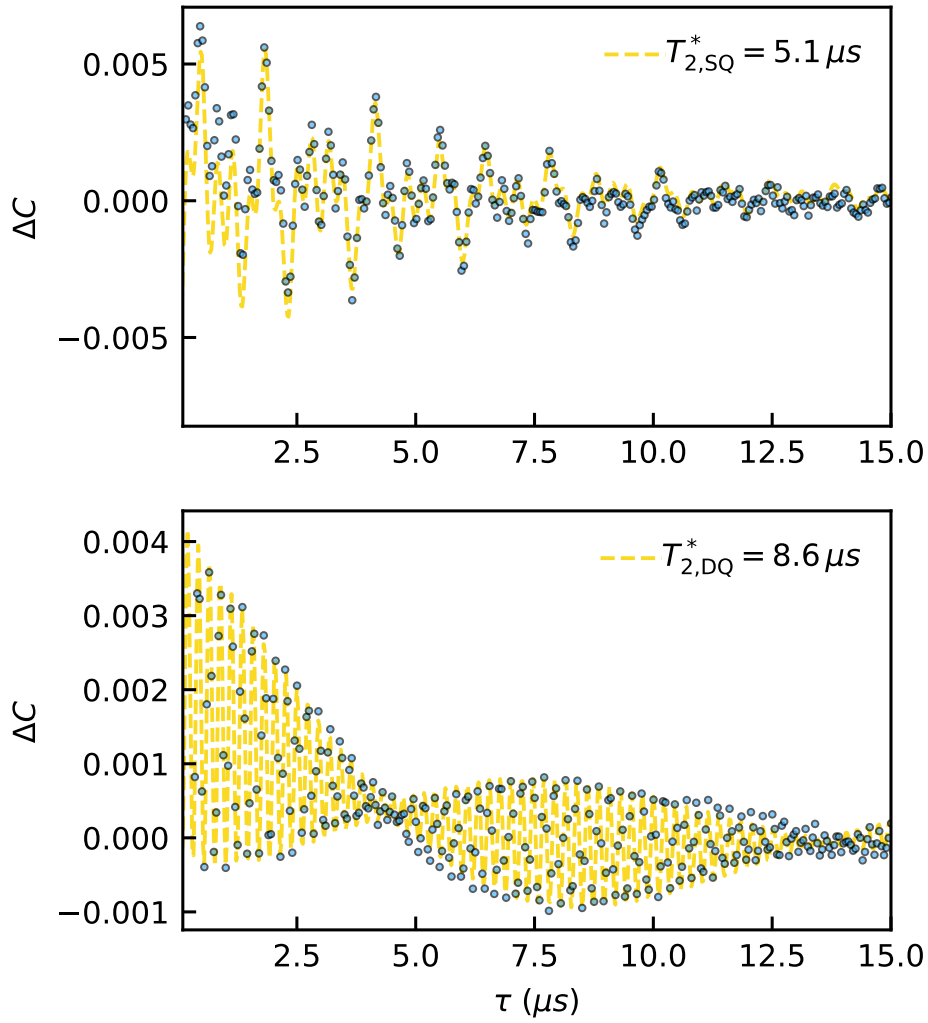


Figure S2. Single-quantum (SQ) and double-quantum (DQ) Ramsey measurements and fits yield the ensemble NV spin dephasing times $T^*_{2,\mathrm{SQ}}$ and $T^*_{2,\mathrm{DQ}}$ at a high-birefringence region (area B of sample 10, see main text Fig. 2). The reduced $T^*_{2,\mathrm{SQ}}$ reflects the strong local strain variation, while the DQ protocol mitigates these effects. ΔC is the change in NV PL contrast.

substitutional nitrogen, with typically one nitrogen atom per NV^0 and two per NV^- center (Barry et al., 2020). Therefore, the post-treatment substitutional nitrogen concentration $[\mathrm{N}_\mathrm{s}^0] \approx 0.35$ ppm. Residual $^{13}\mathrm{C}$ concentration is 0.01% (equivalent to 108 ppm) given the isotopic purification used in the CVD process. Using these values, we estimate the spin-bath-limited NV spin dephasing time to be $T^*_{2,\mathrm{bath}} \approx 20\,\mu$s, slightly larger than the experimentally measured value for a single quantum (SQ) Ramsey measurement (see main text).

5 INCREASING SENSOR SIZE FOR BULK NV ENSEMBLE SENSING

For photon-shot-noise-limited Ramsey-based DC magnetic sensing for an NV ensemble (main text Eq. 1), optimal sensitivity typically occurs when the NV spin free-precession time (τ) is close to the spin dephasing time T_2^* (i.e., $\tau \approx T_2^*$) (Barry et al., 2020). Consequently, the relationship between sensitivity (η) and spin

dephasing time can be approximated as:

$$\eta \propto \frac{\sqrt{T_2^* + t_O}}{T_2^*}, \tag{S2}$$

In the limit of large experimental overhead time ($t_O \gg T_2^*$), sensitivity scales inversely with dephasing time ($\eta \propto 1/T_2^*$). Conversely, when overhead time is negligible ($t_O \ll T_2^*$), sensitivity scales with the inverse square root of dephasing time ($\eta \propto 1/\sqrt{T_2^*}$)

Thus, when evaluating the impact of spatially varying diamond strain on sensitivity through its effect on spin dephasing time (main text Eq. 2), the most conservative scenario is considered. In this scenario, any degradation in dephasing time due to higher strain variation across an increased sensor volume directly worsens sensitivity, following the inverse-linear scaling relationship ($\eta \propto 1/T_2^*$).

6 NV SPIN POLARIZATION DYNAMICS MODELING

We model the NV spin population dynamics under green laser excitation using a simplified five-level system (Schloss, 2019). This modeling supports our experimental calibration and and conversion of laser power to incident optical excitation intensity by simulating NV spin initialization times as functions of laser intensity.

The NV electronic and spin energy levels included in the simulation are illustrated schematically in Fig. S3. The spin-conserving radiative decay rate is set to $\Gamma = 0.67\,\mu\text{s}^{-1}$ (Schloss, 2019). Transitions between excited and singlet states, as well as subsequent transitions to the ground state, are characterized by decay rates given by $\kappa_{ij}\Gamma$, where i, j denote the initial and final states, respectively. The optical excitation rate from the ground to the excited state is modeled as $s\Gamma$, with saturation parameter $s = I/I_{sat}$, where I is the laser intensity and I_{sat} is the NV saturation intensity. The saturation intensity is taken to be approximately $1 - 3\,\text{mW}/\mu\text{m}^2$ (Barry et al., 2020), providing bounds for our simulations. The rate-constant prefactors κ used in the model are averaged from experimental values summarized in Ref. (Schloss, 2019): $\kappa_{45} = 1, \kappa_{35} = 1/7, \kappa_{52} = 1/50, \kappa_{51} = 1/25$.

For the experimental measurement protocol described in the main text (Fig. 6), we simulate NV spin population dynamics starting from the initial states $m_s = 0$ and $m_s = \pm 1$. The following system of coupled first-order differential equations describes the population n_i of each of the five modeled NV states:

$$\begin{aligned}
dn_1/dt &= \Gamma(-sn_1(t) + n_3(t) + \kappa_{51}n_5(t)) \\
dn_2/dt &= \Gamma(-sn_2(t) + n_4(t) + \kappa_{52}n_5(t)) \\
dn_3/dt &= \Gamma(sn_1(t) - (1 + \kappa_{35})n_3(t)) \\
dn_4/dt &= \Gamma(sn_2(t) - (1 + \kappa_{45})n_4(t)) \\
dn_5/dt &= \Gamma(\kappa_{35}n_3(t) + \kappa_{45}n_4(t) - (\kappa_{51} + \kappa_{52})n_5(t)).
\end{aligned} \tag{S3}$$

The simulated PL emission rate is calculated as:

$$R(t) = \Gamma(n_3(t) + n_4(t)), \tag{S4}$$

and is further processed by a low-pass filter (4th-order Butterworth with -3dB cutoff at 1.7 MHz) to mimic the effect of data acquisition hardware used experimentally (NI DAQ USB-6363).

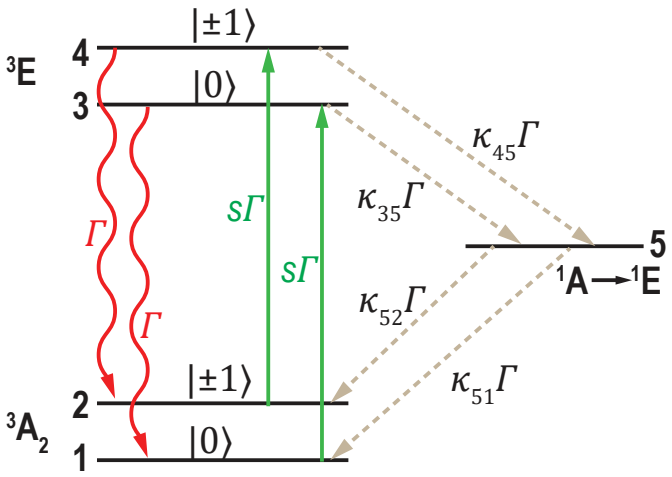


Figure S3. Schematic of the simplified five-level NV photophysics model used in spin polarization dynamics simulations.

The stimulated PL contrast is determined by normalizing the PL trace for spins initialized in the $m_s = \pm 1$ state by the PL for spins initialized in the $m_s = 0$ state. An exponential fit is applied to the PL contrast decay, with the initialization time (t_I) defined as the delay time (t_{delay}) at which the contrast decays to $1/e^3$ of its peak value, consistent with the experimental approach described in the main text.

7 ADDITIONAL RAMSEY MEASUREMENTS ON A SECOND LOW-[N_s^0] DIAMOND

Single-quantum (SQ) confocal Ramsey measurements are performed on a second low-[N_s^0] diamond grown in the same CVD synthesis run. Measurements are taken at five locations across the sample, yielding an average NV ensemble dephasing time of $T^*_{2,\mathrm{SQ}} = 16.9(7)$ μs. Example data from one location is shown in Fig. S4, where the extracted dephasing time is $T^*_{2,\mathrm{SQ}} = 17.3 \pm 1.1$ μs. The measured NV spin dephasing time for this sample is comparable to that of Sample 10 discussed in the main text, confirming similar spin-bath-limited behavior. The consistent nitrogen incorporation and comparable strain homogeneity observed across all the diamonds indicate good batch uniformity and reproducibility of NV ensemble spin properties.

REFERENCES

Barfuss, A., Kasperczyk, M., Kölbl, J., and Maletinsky, P. (2019). Spin-stress and spin-strain coupling in diamond-based hybrid spin oscillator systems. *Physical Review B* 99, 174102

Barry, J. F., Schloss, J. M., Bauch, E., Turner, M. J., Hart, C. A., Pham, L. M., et al. (2020). Sensitivity optimization for NV-diamond magnetometry. *Rev. Mod. Phys.* 92, 015004. doi:10.1103/RevModPhys.92.015004

Cuenca, J. A., Mandal, S., Thomas, E. L., and Williams, O. A. (2022). Microwave plasma modelling in clamshell chemical vapour deposition diamond reactors. *Diamond and Related Materials* 124, 108917

Edmonds, A. M., Hart, C. A., Turner, M. J., Colard, P.-O., Schloss, J. M., Olsson, K. S., et al. (2021). Characterisation of CVD diamond with high concentrations of nitrogen for magnetic-field sensing applications. *Mater. Quantum Technol.* 1, 025001. doi:10.1088/2633-4356/abd88a

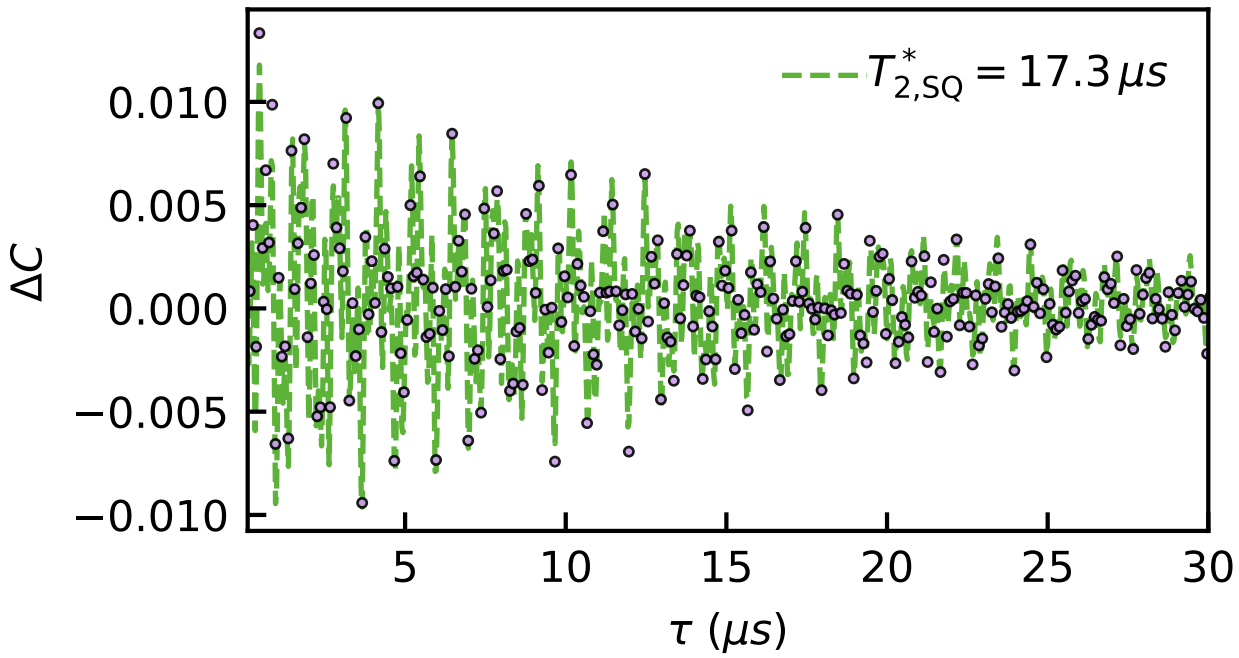


Figure S4. Single-quantum (SQ) Ramsey measurement at one location from a second low-[N_s^0] diamond grown in the same CVD synthesis run. The fitted ensemble NV spin dephasing time is $T^*_{2,\mathrm{SQ}} = 17.3 \pm 1.1\ \mu$s. ΔC is the change in NV PL contrast.

Gracio, J., Fan, Q., and Madaleno, J. (2010). Diamond growth by chemical vapour deposition. *Journal of Physics D: Applied Physics* 43, 374017

Hart, C. A., Schloss, J. M., Turner, M. J., Scheidegger, P. J., Bauch, E., and Walsworth, R. L. (2021). N–diamond magnetic microscopy using a double quantum 4-ramsey protocol. *Phys. Rev. Appl.* 15, 044020. doi:10.1103/PhysRevApplied.15.044020

Kehayias, P., Turner, M. J., Trubko, R., Schloss, J. M., Hart, C. A., Wesson, M., et al. (2019). Imaging crystal stress in diamond using ensembles of nitrogen-vacancy centers. *Phys. Rev. B* 100, 174103. doi:10.1103/PhysRevB.100.174103

Schloss, J. M. (2019). *Optimizing nitrogen-vacancy diamond magnetic sensors and imagers for broadband sensitivity*. Ph.D. thesis, Massachusetts Institute of Technology